Chem Europ
European C Societies P

Check for updates

VIP *Very Important Paper*

Oxygen Reduction and Evolution on Ni-modified Co_3O_4(111) Cathodes for Zn–Air Batteries: A Combined Surface Science and Electrochemical Model Study

Florian Buchner+,[a] Markus Eckardt+,[a, b, c] Timo Böhler,[a] Jihyun Kim,[a] Jasmin Gerlach,[a] Johannes Schnaidt,[b, c] and R. Jürgen Behm*[a, b]

The performance of structurally and chemically well-defined Ni-free and Ni-modified single-crystalline Co_3O_4(111) thin-film electrodes in the oxygen reduction and evolution reactions (ORR and OER) was investigated in a combined surface science and electrochemistry approach. Pure and Ni-modified Co_3O_4(111) film electrodes were prepared and characterized under ultrahigh-vacuum conditions by scanning tunneling microscopy and X-ray photoelectron spectroscopy. Both Ni decoration (by post-deposition of Ni) and Ni doping (by simultaneous vapor deposition of Ni, Co, and O_2) induced distinct differences in the base cyclic voltammograms in 0.5 M KOH at potentials higher than 0.7 V compared with Co_3O_4(111) electrodes. Also, all oxide film electrodes showed a higher overpotential for the ORR but a lower one for the OER than polycrystalline Pt. Ni modification significantly improved the ORR current densities by increasing the electrical conductivity, whereas the OER onset of approximately 1.47 V_{RHE} (RHE: reversible hydrogen electrode) at 0.1 mA cm^{-2} was almost unchanged.

Introduction

During the last decades, post-Li-ion energy-storage technologies such as secondary Zn–air batteries have been discussed as attractive alternatives for future battery cells. In particular rechargeable Zn–air batteries have attracted much attention as promising candidates for electrochemical energy storage[1–8] owing to their high energy density (1086 W h kg^{-1}), high safety, environmental friendliness, and economic viability.[4] Nevertheless, their further development is challenging. A particular challenge is the improvement of the slow kinetics of the oxygen reduction reaction (ORR) and the oxygen evolution reaction (OER) at the air cathode. This calls for the development of more efficient bifunctional catalysts. So far, a broad range of materials, such as noble metals and their alloys, carbon-based materials, nitrogen-doped intermetallic compounds, and transition-metal oxides such as perovskites and spinels have been investigated.[9–16] In particular spinel-type cobalt oxides (Co_3O_4)[10,11] and mixed metal oxides[15,16] were identified as promising materials for low-cost bifunctional electrocatalysts for the ORR/OER. Furthermore, the combination of two metals such as Co and Ni in mixed oxides was claimed to have favorable effects on the activity.[17,18]

Although there are a number of studies on the ORR/OER characteristics of these realistic materials, little is known about the surface structure of these electrode materials on an atomic scale and the correlation between the local structure and electrocatalytic properties of these materials in the ORR/OER. This is the topic of the present work, in which we report the results of a combined surface science and electrochemical study on the preparation of structurally and chemically well-defined pure Co_3O_4, Ni-decorated Co_3O_4, and Ni-doped spinel-type Co_3O_4 films, such as $Ni_{1.0}Co_{2.0}O_4$, their electrochemical characteristics, and their electrocatalytic properties in the ORR/OER. We were particularly interested in the influence of Ni decoration and Ni doping on the electrochemical/electrocatalytic properties of these films. Hence, we explored two types of Ni-modified thin films: 1) Co_3O_4 films decorated with submonolayer amounts of Ni, combining the properties of both materials at the interface, and 2) mixed Ni- and Co-containing (Ni-doped) thin films. The single-crystalline Ni-free and Ni-modified Co_3O_4 thin-film model electrodes with film thicknesses of approximately 6–9 nm were grown on a single-crystalline Ir(1 0 0)-(2×1)O/Ir(1 0 0)-(3×1)O surface under ultrahigh vacuum (UHV) and characterized by scanning tunneling microscopy (STM) as

[a] Dr. F. Buchner,+ Dr. M. Eckardt,+ T. Böhler, Dr. J. Kim, J. Gerlach, Prof. Dr. R. J. Behm
Institute of Surface Chemistry and Catalysis
Ulm University
Albert-Einstein-Allee 47, 89081 Ulm (Germany)
E-mail: juergen.behm@uni-ulm.de

[b] Dr. M. Eckardt,+ Dr. J. Schnaidt, Prof. Dr. R. J. Behm
Helmholtz Institute Ulm Electrochemical Energy Storage (HIU)
Helmholtzstrasse 11, 89081 Ulm (Germany)

[c] Dr. M. Eckardt,+ Dr. J. Schnaidt
Karlsruhe Institute of Technology (KIT)
P.O. Box 3640, 76021 Karlsruhe (Germany)

[+] These authors contributed equally to this work.

Supporting Information and the ORCID identification number(s) for the author(s) of this article can be found under: https://doi.org/10.1002/cssc.202000503.

© 2020 The Authors. Published by Wiley-VCH Verlag GmbH & Co. KGaA. This is an open access article under the terms of the Creative Commons Attribution Non-Commercial License, which permits use, distribution and reproduction in any medium, provided the original work is properly cited and is not used for commercial purposes.

 © 2020 The Authors. Published by Wiley-VCH Verlag GmbH & Co. KGaA, Weinheim

well as X-ray and ultraviolet photoelectron spectroscopy (XPS and UPS). Their electrochemical/electrocatalytic properties were characterized by electrochemical measurements under conditions of continuous, controlled electrolyte mass transport in a combined UHV–electrochemistry setup. This setup, which is essentially identical to that described previously by Schnaidt et al.,[19] allows us to transfer the electrodes from UHV into an electrochemical cell without contact to air.

In general, there are only few reports on electrochemical investigations using well-ordered oxide electrodes. These include studies on the stability and electrocatalytic performance of Fe_3O_4(001) and (110) single crystals in the OER in 1 M NaOH by Müllner et al.,[20] the OER on atomically defined CoO_x nanoislands on Au(111) in 0.1 M NaOH by Fester et al.,[21] and the pH-dependent stability of Co_3O_4(111) thin-film model electrodes in phosphate buffer by Faisal et al.[22] To the best of our knowledge, such model studies exploring molecular/atomic-level details of the ORR/OER on well-defined pure or Ni-doped cobalt oxide thin films have not been reported so far.

Before presenting and discussing the results, we briefly summarize the results of previous studies relevant to this work. Liang et al.[23] observed a promising ORR onset at approximately 0.88 V versus reversible hydrogen electrode (RHE) in alkaline electrolyte as well as an OER onset at lower potentials than on Pt/C for Co_3O_4 nanocrystals supported on graphene in rotating ring disk electrode measurements. Cation modification of Co_3O_4 by Ni[17,18] and Mn,[24] forming a mixed oxide, was shown to further decrease the OER[17,18,24] and ORR[18,24] overpotentials compared to those on unmodified Co_3O_4.[17,18,24] Furthermore, Prabu et al.[18] reported that the ORR and OER onsets and current densities depend on the structure of the mixed oxides and show the best ORR/OER activity for a $NiCo_2O_4$ catalyst with a 1D structure and optimized access for the electrolyte, with an improvement in the onset potential by approximately 30 mV. Recently, Singhal et al.[17] obtained enhanced OER activity by using Ni-doped Co_3O_4 particles. They explained this improvement by a higher surface oxygen (lattice oxygen) concentration compared with pure Co_3O_4 because terminal OH or O can be active for the OER depending on the potential.[25]

In the following we first briefly describe the experimental setup and procedures, followed by the characterization of freshly prepared Co_3O_4(111) films by XPS, UPS, and STM. In the following sections we focus on the preparation and characterization of Ni-modified Co_3O_4(111) films, which were prepared by 1) post-deposition of Ni on a Co_3O_4(111) thin film or 2) by simultaneous vapor deposition of Ni and Co in an O_2 atmosphere on an Ir(100)-(2×1)O/Ir(100)-(3×1)O substrate. Then, we present a quantitative analysis of the XP spectra and deal with the base cyclic voltammograms (BCVs) and the ORR/OER characteristics of these films. Finally, the main findings and insights of this study are summarized. Overall, this work provides an atomic/molecular-scale picture of the correlation between surface structure and surface chemistry of model cathodes with activity, which is considered to be an essential step towards the development of suitable bifunctional catalyst for air cathodes in Zn–air batteries.

Experimental Section

The experiments were performed in a commercial UHV system (SPECS) with a base pressure of 2×10^{-10} mbar. It consisted of two chambers, one containing an Aarhus-type STM/atomic force microscopy (AFM) system (SPECS Aarhus SPM150 with a Colibri sensor), and the other equipped with an X-ray source (SPECS XR50, AlK_α and MgK_α), an He lamp (SPECS UVS 300), and a hemispherical analyzer (SPECS, DLSEGD-Phoibos-Has3500) for XPS and UPS measurements.

Co_3O_4(111) thin films were prepared on an Ir(100) substrate from MaTecK (purity 99.99%, surface roughness <0.01 μm, orientation accuracy <0.1°), by following procedures described in the literature.[26–28] Following Kresimir et al.,[29] the Ir(100) sample was cleaned by Ar^+ sputtering (1.7 keV, RT), annealing to 1370 K (4 min), and O_2 adsorption at 870 K in 5×10^{-7} O_2 (10 min). In the second step the sample was heated to 1370 K under UHV (6 min) and subsequently cooled from 870 K to approximately RT in an O_2 atmosphere (5×10^{-7} mbar), followed by a final flash annealing to 780 K in UHV, which [as previously verified by low energy electron diffraction (LEED) measurements][26,27,29] resulted in a well-ordered Ir (100)-(2×1)O surface [note that, in addition, we observed Ir (100)-(3×1)O; see below]. Afterwards, the Co_3O_4(111) thin films were grown on Ir(100)-(2×1)O/ Ir(100)-(3×1)O by vapor deposition of metallic Co (Tectra twin pocket dual mini e-beam evaporator, equipped with 2 mm 99.995% Co rod from Alfa Aesar, $I_{flux}\approx20$ nA, $I_{emission}\approx25$ mA, $U\approx1375$ V) in a background atmosphere of O_2 [oxygen 6.0, Air Liquide, $(6–8)\times10^{-6}$ mbar] at RT. The evaporation rate of Co was approximately 4–6 Å min^{-1}, as estimated from the film thickness (6–9 nm) and evaporation time (15 min). After deposition, the films were annealed in an O_2 atmosphere [$(6–8)\times10^{-6}$ mbar] at approximately 520 K for 5 min and afterwards in UHV at approximately 570 K for 2 min. This preparation procedure resulted in clean Co_3O_4(111) films, as determined by angle-resolved XPS measurements of the Co 2p, O 1s, and Ir 4f regions. The film thickness of approximately 6–9 nm was derived from the almost complete attenuation of the Ir 4f intensity at normal emission.

For the generation of Ni-doped Co_3O_4(111) films we followed two routes using the two compartments of the dual e-beam evaporator [first compartment: Co (see above), second compartment: Ni rod, 2 mm diameter, Alfa Aesar 99.995%]: 1) post-deposition of small amounts of Ni^0 [>0.2 monolayer equivalents (MLE)] onto a Co_3O_4(111) film, with the sample at RT, and 2) simultaneous vapor deposition of Co^0 and Ni^0 at an O_2 background pressure of $(6–8)\times10^{-6}$ mbar at RT.

For the UPS measurements (He I: $h\nu=21.2$ eV) at normal emission (0° to the surface normal), a bias voltage of −5.0 V was applied to the sample to accelerate the photoelectrons into the analyzer (pass energy $E_{pass}=1$ eV), which allowed us to determine a clear electron cutoff and its energy (E_{cutoff}).

For the XPS measurements we used an MgK_α X-ray source (1253.6 eV), operated at a power of 250 W ($U=14$ kV, $I=17.8$ mA). XP spectra were recorded at $E_{pas}=100$ eV at normal and grazing emission (0 and 70° to the surface normal, respectively). For fitting the XP spectra we used the Igor Pro 8.03 software, which includes a simultaneous fit of background (Shirley+slope) and signal, by applying an asymmetric pseudo-Voigt-type function. The thickness of the post-deposited Ni was calculated from the damping of the Co 2p and O 1s substrate peaks. Here, we assumed that an MLE of Ni has a thickness of $d\approx2$ Å,[30] equivalent to the (111) interplanar distance. The Ni film thickness d was calculated by $I_d=I_0\exp(-d/\lambda\cos\theta)$ ($I_d=$ substrate peak intensity before Ni deposition, $I_0=$in-

© 2020 The Authors. Published by Wiley-VCH Verlag GmbH & Co. KGaA, Weinheim

tensity after Ni deposition, θ = emission angle with respect to the surface normal), with electron inelastic mean free paths λ of the Co 2p and O 1s electrons (kinetic energies ≈470 and 720 eV, respectively) for Ni of 9 and 12 Å, respectively.[31]

For the electrochemical measurements, freshly prepared, well-defined samples were transferred from the UHV chamber (≈2×10^{-10} mbar) to a load lock chamber (≈2×10^{-8} mbar), which was subsequently flooded with N_2. The electrochemical cell was a dual thin-layer flow cell, which could be moved into the load lock chamber (N_2 flushed) through a CF quick access door and brought into contact with the freshly prepared sample by a lifting platform. The flow cell largely resembled our dual thin-layer flow cell design reported earlier.[19,32,33] For the electrochemical measurement we used an RHE as reference and a Pt-wire counter electrode. Current densities were calculated from the geometric area of the sample of 0.196 cm^2. The potential was controlled by a BioLogic (SP-300) potentiostat. A 0.5 M KOH solution (Merck Emsure for analysis in MilliQ water, 18.2 MΩ cm, pH_{KOH} 13.7), saturated with N_2 (Westfalen Gas, 5.0) or O_2 (Westfalen Gas, 6.0) was used as electrolyte. For the electrochemical measurements, we first acquired BCVs of the thin-film model electrodes with a scan rate of 100 mV s^{-1} until stable, unchanged CVs were reached (≈20 cycles). Then, we decreased the rate to 10 mV s^{-1} for a few cycles (see Figure 9), followed by the ORR and OER measurements. The CVs showed moderate changes in the first few cycles (if these could be directly recorded after bringing the cell into contact with the sample), and they remained stable after a few cycles. Therefore, some initial changes at the interface cannot be ruled out. The electrolyte flow for the ORR and OER measurements (0.5 mL min^{-1}) was controlled by a Harvard Apparatus 11 Plus.

Results and Discussion

To elucidate possible effects of the underlying Ir substrate on the electrochemical measurements on thin oxide films, we first characterized the Ir surface by STM (Figure 1a) and cyclic voltammetry (Figure 1b). Large-scale STM images (see Figure 1a) show parallel lines with different apparent heights. According to the literature,[34] these lines result from reconstruction of the surface. A more detailed view of the atomic structure is possible in the atomic-resolution STM image in the inset in Figure 1a, which shows parallel rows of individual round protrusions (distance of ≈2.7 Å) with a distance between the lines of approximately 8 Å. The lattice vectors of the resulting unit cell are $|\vec{a}| = 8.1\pm0.03$ Å, $|\vec{b}| = 2.7\pm0.01$ Å, $\alpha = 90\pm3°$, which correspond to a (3×1)-O structure. Other STM images (not shown here) resolved a local (2×1)-O structure. Hence, both phases seem to coexist. More details of the structure and ordering of oxygen on Ir(1 0 0) can be found in the literature.[34]

The corresponding BCV (Figure 1b) recorded on such a surface in 0.5 M KOH shows distinct signals at approximately 0.25 V in the cathodic and at approximately 0.30 V in the anodic scan. In addition, there are a number of much smaller signals between 0.0 and 0.4 V. All of these peaks were attributed to hydrogen adsorption and desorption, respectively.[35] The highly ordered structure of the Ir(1 0 0) surface with very few defect sites results in the very sharp main peaks at 0.25 and 0.30 V. The signals at approximately 0.6 V in the anodic and the cathodic scan were attributed to the reversible adsorption/desorption of OH^- on the surface, as stated by Pajkossy et al.[35] Close to 0.0 V we find the beginning of the hydrogen evolution reaction (HER), and above 1.4 V the OER starts, forming oxygen through water splitting. Overall, the CV shows the typical hydrogen and OH^- adsorption/desorption features presented by Pajkossy et al.[35] and no indication of surface oxidation and reduction.

For comparison with the Ni-induced features in the BCVs of Ni-modified Co_3O_4 thin films (see below), we also recorded BCVs after deposition of approximately 3 MLE of Ni^0 on Ir(1 0 0)-(3×1) (Figure 1b, green line). The anodic scan now shows an additional feature at approximately 1.46 V, which corresponds to the oxidation of surface $Ni(OH)_2$ to NiOOH (Ni^{2+} to Ni^{3+}); the corresponding reduction peak is found at approximately 1.37 V in the cathodic scan.[36,37] The peak pairs attributed to hydrogen and OH^- adsorption/desorption are much less intense than those obtained on the pristine surface, that is, a small part of the Ir(1 0 0) substrate is still accessible to the electrolyte.

Structure and composition of Co_3O_4(1 1 1) films on Ir(1 0 0)-(2×1)O/ Ir(1 0 0)-(3×1)O

First, we characterized Co_3O_4(1 1 1) thin films prepared on a Ir(1 0 0)-(2×1)O/Ir(1 0 0)-(3×1)O substrate ($d_{Co_3O_4}$ ≈6–9 nm) by XPS, UPS (Figure 2), and STM (Figure 3). Angle-dependent XPS was performed at emission angles of 0 and 70° with respect to the surface normal, which in the following are termed as normal emission ["bulk-sensitive", extended surface region, information depth (ID) ≈6–9 nm] and grazing emission ("surface-sensitive", near-surface region, ID = 1.5–3 nm).

The Co_3O_4 film was generated by vapor deposition of Co^0 in an O_2 atmosphere [(6–8)×10^{-6} mbar], as described in detail in the Experimental Section. In general, spinel-type Co_3O_4 has both octahedral Co^{3+} and tetrahedral Co^{2+} centers ($Co^{2+}Co_2^{3+}O_4$). The normal-emission Co 2p spectrum (ID = 6–9 nm) of the spinel Co_3O_4(1 1 1) thin film in Figure 2a shows typical features of such film surfaces, with two asymmetric main peaks (doublet), which are related to Co^{2+} and Co^{3+} states, and a satellite structure for each of these peaks (see Biesinger et al.)[38]. This is clearly different

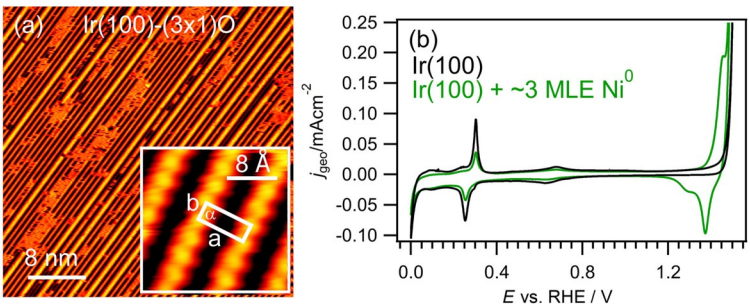

Figure 1. a) STM image of an ordered Ir (1 0 0)-(3×1)O surface with the unit cell indicated in the inset and b) corresponding CV of Ir (black solid line) and after deposition of approximately 3 MLE of Ni (green solid line) recorded in N_2-saturated 0.5 M KOH (10 mV s^{-1}).

© 2020 The Authors. Published by Wiley-VCH Verlag GmbH & Co. KGaA, Weinheim

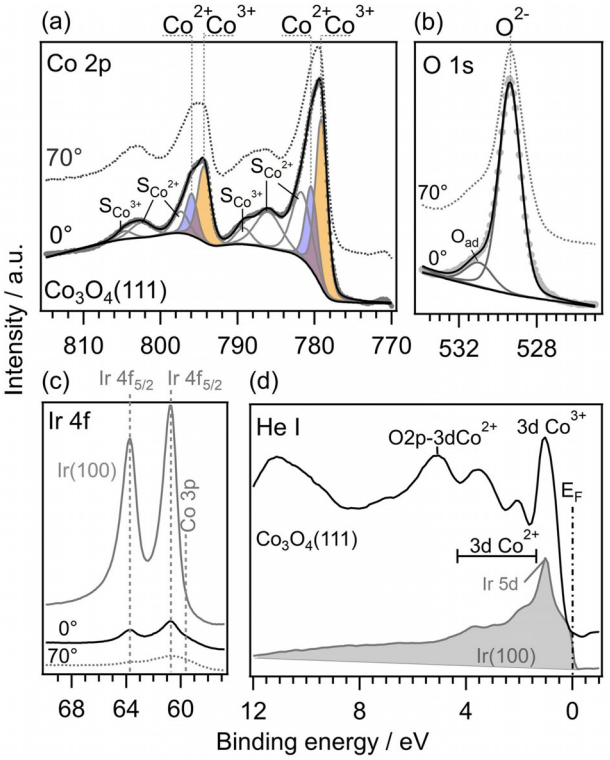

Figure 2. (a–d) XPS and UPS measurements recorded on a Co_3O_4(111) thin film (6–9 nm) on Ir(100)-(2×1)O.

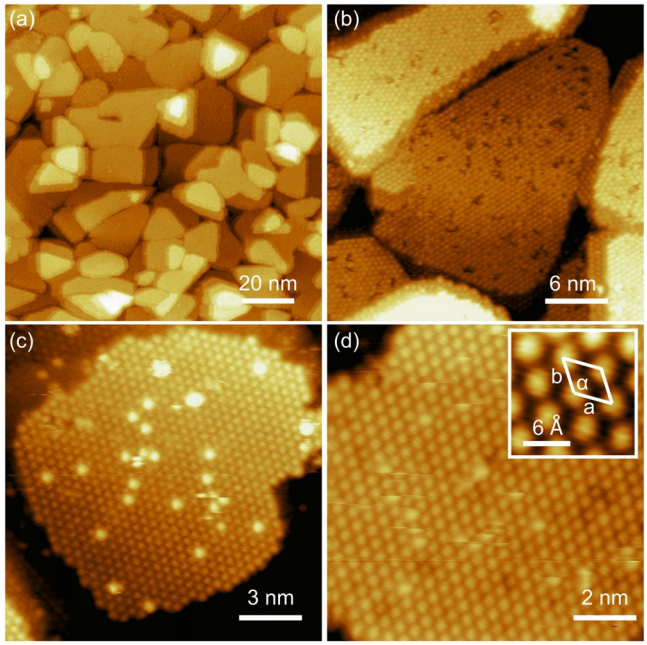

Figure 3. (a–d) STM images of a Co_3O_4(111) thin film (6–9 nm) on Ir(100)-(2×1)O. The large-scale STM image in (a) shows flat island structures. At a smaller scale (b–d) atoms could be resolved on these islands. The inset in (d) shows an atomic-resolution STM image with indication of the unit cell ($a=b=5.7$ Å, $\alpha=120°$). Tunneling parameters: a) $I=50$ pA, $U=-1.8$ V; b) $I=50$ pA, $U=-1.8$ V; c) $I=20$ pA, $U=-2.3$ V; d) $I=20$ pA, $U=-2.3$ V.

from the Co 2p signal of rock salt CoO (see Refs. [38,39]). Deconvolution of the Co 2p spectrum (Figure 2a) by peak fitting leads to the following result: the doublet at 780.4 (Co $2p_{3/2}$) and 796.0 eV (Co $2p_{1/2}$) (shaded blue) is assigned to Co^{2+} states together with two satellites for each peak ($S_{Co^{2+}}$) at approximately 782, 786 and 797, 802 eV, respectively.[38,39] According to the literature, the satellites are typical for late 3d transition-metal monoxides with partially filled e_g character.[40] In addition, the Co 2p spectrum shows a doublet at 779.1 (Co $2p_{3/2}$) and 794.4 eV (Co $2p_{1/2}$) (shaded orange), which is assigned to Co^{3+} states, together with one satellite for each peak ($S_{Co^{3+}}$) at approximately 789 and 805 eV, respectively.[38] The ratio of the peak intensities of the Co^{3+}/Co^{2+} peaks is 2:1, in perfect agreement with the nominal concentrations of these species in $Co^{2+}Co_2^{3+}O_4$. The O 1s region (Figure 2b) exhibits a main peak at 529.4 eV, which results from O^{2-} anions, and a low-intensity shoulder at the high-binding-energy (BE) side (O_{ad}), which we assign to a small number of adsorbed oxygen atoms. The ratio of the normalized peak intensities of the O 1s state, based only on the main peak, and of the Co 2p region is approximately 1.3, considering the atomic sensitivity factors of the O 1s (0.63) and Co 2p (4.5) signals, which matches with the expected nominal ratio. Furthermore, the grazing-emission Co 2p spectrum (dashed line, ID = 1.5–3 nm) closely resembles the normal-emission spectrum, which demonstrates that Co_3O_4(111) is present both in the near- and extended surface regions.

The normal-emission Ir 4f spectrum (Figure 2c) recorded on pristine Ir (gray solid line) shows the Ir $4f_{5/2}$ and Ir $4f_{7/2}$ substrate peaks at 63.8 and 60.8 eV, respectively. After deposition of the Co_3O_4(111) film on Ir(100)-(2×1)O (black solid line), they have almost completely disappeared, which allows for calculation of the film thickness ($d\approx$6–9 nm, see the Experimental Section). In grazing emission (gray dashed line), the Ir substrate peaks are essentially absent. In addition, a low-intensity contribution from a Co 3p signal appears at 0 and 70° emission.

The valence-band spectra recorded before and after deposition of the Co_3O_4 film are shown in Figure 2d. For the UPS measurement we used the He I line (photon energy of ≈21.21 eV). The Fermi energy E_F (gray solid line, shaded gray) is marked by a dash-dotted line. The electronic state at approximately 1.0 eV is assigned to emission from the Ir 5d orbital. After deposition of the Co_3O_4 film (d = 6–9 nm), this feature completely disappears owing to damping by the oxide thin film. Instead, new features arise, which have previously been discussed by Chuang et al.[41] According to these authors the peak at approximately 1.5 eV is related to emission from a Co^{3+} 3d state, and the bands between 2–5 eV are assigned to Co^{2+} 3d states. The feature at approximately 6 eV is attributed to O 2p-derived states or mixed O 2p–Co 3d states. Very similar UP spectra were reported also by Langell et al.[42] for a Co_3O_4 film on CoO. In total, both the Co 2p and O 1s core-level spectra (Figure 2a,b) and the valence-band spectrum (Figure 2d) are in excellent agreement with the expected spectra for Co_3O_4 surfaces.

Beside the spectroscopic measurements we also performed STM measurements for structural characterization (Figure 3). Typical STM images recorded on a Co_3O_4(111) film are shown in Figure 3a–d. The large-scale STM image in Figure 3a reveals

© 2020 The Authors. Published by Wiley-VCH Verlag GmbH & Co. KGaA, Weinheim

extended flat island structures, the longer diameters of which range between approximately 10 and 60 nm. The maximum height differences in such images are approximately 8 Å, and the height differences between the top levels of neighboring islands are in the range of 2–5 Å. The higher-resolution STM images in Figure 3 b–d resolve the atomic structure on top of the islands. According to Meyer et al.,[27] the surface is most likely determined by Co^{2+} cations, which are visible in the STM images. In addition, Figure 3 b shows a number of holes, which, considering the recent report that these surfaces are Co^{2+}-terminated,[27] may be related to missing Co^{2+} cations. In contrast, the STM image in Figure 3 c shows protrusions on top of the islands under very similar tunneling conditions [b) $I=50$ pA, $U=-1.8$ V; c) $I=20$ pA, $U=-2.3$ V]. We interpret these differences as tip effects, caused by different structural/electronic properties of the apex of the STM tip. Finally, in the atomic-resolution STM images in Figure 3 d, we indicate the unit cell of this surface. It is characterized by lattice vectors $|\vec{a}|=|\vec{b}|=0.57\pm0.03$ nm, which enclose an angle of $\alpha=120\pm5°$, in excellent agreement with results in previous reports.[26,27,43,44]

Post-deposition of Ni onto Co_3O_4(111) films on Ir(100)-(2×1)O/Ir(100)-(3×1)O

Having characterized the Co_3O_4(111) thin films on Ir(100)-(2×1)O by XPS, UPS, and STM, the surface was modified by post-deposition of Ni at 300 K sample temperature. The resulting morphological and chemical changes of the Co_3O_4(111) film were characterized by STM (Figure 4 a–d) and XPS (Figure 5).

After post-deposition of approximately 0.5 MLE of Ni^0 onto a pristine Co_3O_4(111) thin film, the STM images in Figures 4 a, b reveal the typical flat island structure observed already for the Co_3O_4(111) film (see Figure 3). In addition, small clusters are resolved, which are homogeneously distributed over the surface and the lateral dimensions of which vary between approximately 0.6 and 1.7 nm (full width at half-maximum), with heights of 0.1–0.35 nm.

The corresponding XP spectra recorded after post-deposition of 0.5 MLE of Ni (Figure 5, light blue curve) show a new signal in the Ni 2p region with maxima at 852.3 and 870.0 eV, which are characteristic for the Ni $2p_{3/2}$ and Ni $2p_{1/2}$ signals of metallic Ni, respectively.[45] At the same time the Co 2p and O 1s signals of Co_3O_4 are damped compared with pristine Co_3O_4 (black solid lines), indicative of adsorbed Ni^0 on top of the Co_3O_4(111) film. The nominal thickness of approximately 1 Å, equivalent to approximately 0.5 MLE of adsorbed Ni^0, was calculated from the damping of the Co 2p and O 1s peaks (≈11 and 8%, respectively; see the Experimental Section). Here we note that this calculation assumes a homogeneous Ni film, which according on the STM images is not the case. Hence, in reality the Ni deposition must be slightly higher to achieve the same damping.

In a second experiment we deposited approximately 2 MLE of Ni^0 onto a pristine Co_3O_4(111) thin film. The STM images (Figure 4 c, d) show clusters of larger size than before, which are also homogeneously distributed over the surface and largely cover the surface. The typical flat island structures of pristine Co_3O_4(111) films (see Figure 1) are, however, still well resolved. The size of the clusters is approximately 4 nm on average, with a density of approximately 0.08 nm^{-2}. The corresponding XP spectra in Figure 5 (red curves) now exhibit more pronounced signals of metallic Ni at 852.3 and 870.0 eV. Again, the Co 2p and O 1s signals are both damped, owing to deposited Ni^0 on top of Co_3O_4(111). From the resulting loss in intensity of the Co 2p and O 1s peaks (≈39 and 30%, respectively) we calculate a nominal Ni film thickness of approximately 4 Å, which corresponds to approximately 2 MLE. Again, the real Ni film thickness must be slightly higher because we assumed a homogeneous Ni film in this cal-

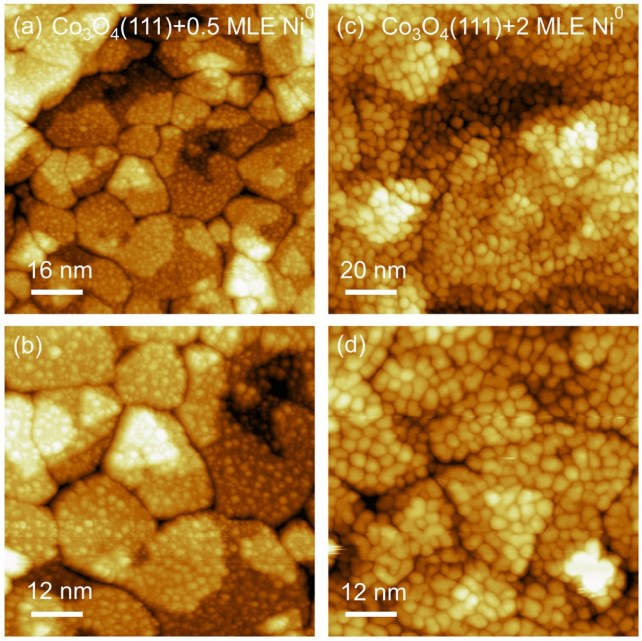

Figure 4. (a–d) STM images of a Co_3O_4(111) film after post-deposition of 0.5 and 2 MLE of Ni^0. Tunneling parameters: a) $I=70$ pA, $U=-2.3$ V; b) $I=50$ pA, $U=-2.5$ V; c) $I=50$ pA, $U=+2.4$ V; d) $I=50$ pA, $U=+2.4$ V.

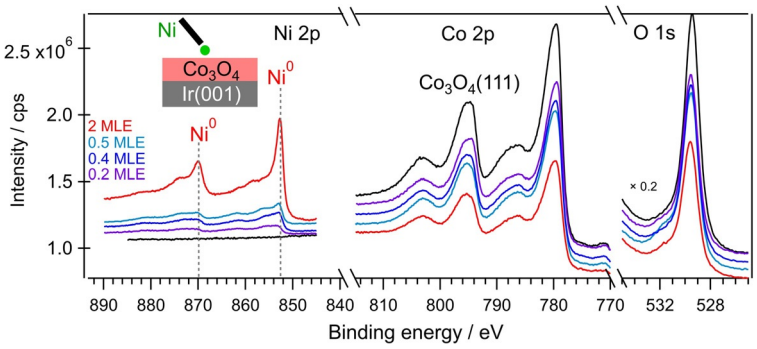

Figure 5. XPS measurements on a Co_3O_4(111) film after post-deposition of 0.2, 0.4, 0.5, and 2 MLE of Ni^0. The intensities of the XP spectra were normalized by the atomic sensitivity factors (Ni 2p: 5.4, Co 2p: 4.5, O 1s: 0.63), otherwise they are shown with the same intensity scale. For better visibility of all spectra, the O 1s peaks were scaled down by a factor of 0.2.

© 2020 The Authors. Published by Wiley-VCH Verlag GmbH & Co. KGaA, Weinheim

culation, which according to the STM images is not the case. A more quantitative evaluation and discussion of the Ni 2p spectra follows below. Overall, the general trend visible in the XP spectra in Figure 5 is the appearance of new Ni^0 states, the intensity of which increases with increasing amount of Ni, together with increasingly damped Co 2p and O 1s signals owing to the deposited Ni^0.

Ni- and Co-containing mixed oxide films on Ir(1 0 0)-(2×1)O/ Ir(1 0 0)-(3×1)O

Next, we changed the preparation route, and Ni and Co were deposited simultaneously in an O_2 atmosphere onto the Ir(1 0 0)-(2×1)O surface (sample temperature 300 K). Typical STM images recorded on the resulting mixed oxide film surface, the composition of which in this case was derived from the XP spectra as $Ni_{1.0}Co_{2.0}O_4$ (see below), are shown in Figure 6a–d. Core-level spectra of the Ni 2p, Co 2p, and O 1s regions recorded on film surfaces with increasing Ni contents, which were prepared by increasing the Ni flux during deposition while keeping the Co flux and the O_2 partial pressure constant, are shown in Figure 7.

The large-scale STM image in Figure 6a reveals extended flat islands with slightly elongated shapes, the long diameters of which range between approximately 10 and 40 nm, essentially similar to our findings for the pristine Co_3O_4 film. In contrast to pristine Co_3O_4 films, however, we now also observed smaller islands (<10 nm in diameter) on top of the flat island structures. The apparent height of the islands with respect to neighboring "holes" (examples are marked by white arrows in Figure 6a) is approximately 1–2 nm, which indicates that the islands are at least several monolayers in height. In addition, the islands are often separated by trenches or "cracks" with an apparent depth of similar magnitude. In contrast, the height difference between the tops of the islands is in the range of 2–8 Å. Hence, the Ir(1 0 0)-(2×1)O/ Ir(1 0 0)-(3×1)O surface is covered by a quasi-continuous film with distinct trenches.

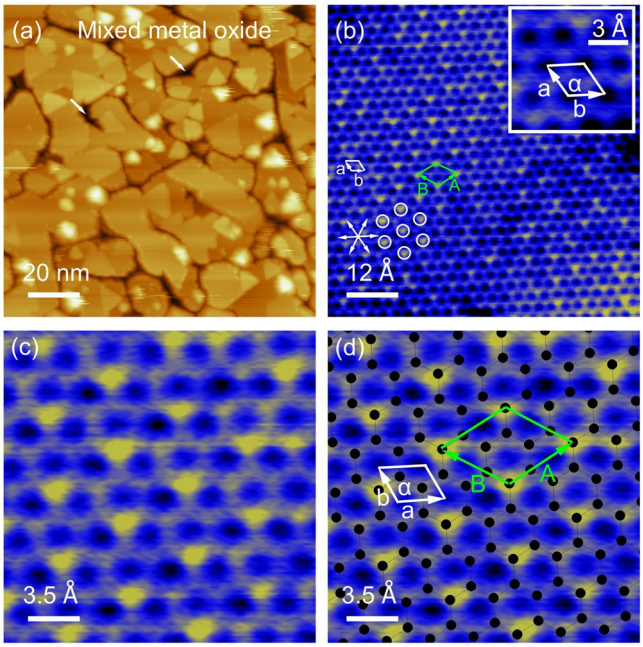

Figure 6. STM images of a $Ni_{1.0}Co_{2.0}O_4$ mixed metal-oxide thin film generated by simultaneous deposition of Co^0 and Ni^0 in an O_2 atmosphere (see the Experimental Section) on Ir(1 0 0)-(2×1)O. The STM images correspond to the sample indicated by the light blue XP spectra in Figure 7. Tunneling parameters: a) $I=90$ pA, $U=+2.3$ V; b), c),d) $I=100$ pA, $U=-777$ mV.

The higher-resolution STM images of the $Ni_{1.0}Co_{2.0}O_4$ surface in Figure 6b–d resolve the atomic surface structure on the islands. These STM images show a much smaller surface lattice than that observed for Co_3O_4(1 1 1) (see Figure 3). The preferential crystallographic directions are marked by white arrows in Figure 3b, and the unit cell with lattice vectors of $|\vec{a}|=|\vec{b}|=0.30\pm0.01$ nm and $\alpha=120\pm5^\circ$ is indicated in the enlarged inset image in Figures 6b and also in Figure 6d. In addition to the honeycomb periodic lattice (superimposed on the surface structure in Figure 6d), some images also reveal patches of additional protrusions, with an ordered short-range structure (see yellow protrusions in Figure 6b, c, some of which are marked by white circles in Figure 6b). They are more clearly visible in the enlarged STM images in Figure 6c, d. These protrusions form a commensurate $\begin{bmatrix} 2 & 1 \\ -1 & 1 \end{bmatrix}$ superstructure relative to the honeycomb structure. The unit cell of the superstructure (marked in green in Figure 6b, d) exhibits lattice vectors of $|\vec{A}|=|\vec{B}|=0.52\pm0.02$ nm and $\alpha=120\pm5^\circ$. The apparent superstructure observed on part of the surface can most simply be explained by Ni-induced modification of the original structure in the mixed oxide layer, whereby we cannot distinguish between Ni and Co in the STM images. Furthermore, in Figure 6b we also see that the superstructure formed by these protrusions is present only on part of the surface, which might indicate the coexistence of two different phases in the film, possibly with different contributions of Ni and Co. The exact structure of these phases, however, is not accessible from these STM measurements.

The Ni 2p, Co 2p, and O 1s core-level XP spectra obtained for different Ni fluxes at constant Co flux and O_2 partial pressure, and hence with different Ni/Co ratios, show a clear trend (Figure 7). Whereas the intensity of the O 1s signals is essentially identical for all of the mixed oxide films, the Co 2p signals decrease in intensity, and the Ni 2p intensity increases, as expected for increasing replacement of Co ions by Ni ions in the film. At first glance, the Co 2p and O 1s spectra are very similar to those obtained on pure Co_3O_4 (black solid lines; see Figure 1). The peak-area analysis of the Ni 2p, Co 2p, and O 1s regions (corrected by the sensitivity factors Ni 2p: 5.4, Co 2p: 4.5, O 1s: 0.63) revealed mixed oxide films with the following stoichiometries with increasing Ni content and decreasing Co content: $Ni_{0.2}Co_{2.8}O_4$, $Ni_{0.5}Co_{2.5}O_4$, $Ni_{0.8}Co_{2.2}O_4$, $Ni_{1.0}Co_{2.0}O_4$, and $Ni_{1.3}Co_{1.7}O_4$, in which the relative precision in the cation composition is approximately 10%. Note that, according to this analysis, the STM measurements in Figure 6 were performed on $Ni_{1.0}Co_{2.0}O_4$. Based on these observations, these films may consist of nickel-doped cobalt oxides with $Ni_xCo_{3-x}O_4$ stoichiometry, in which Co^{3+} and Co^{2+} cations are increasingly re-

© 2020 The Authors. Published by Wiley-VCH Verlag GmbH & Co. KGaA, Weinheim

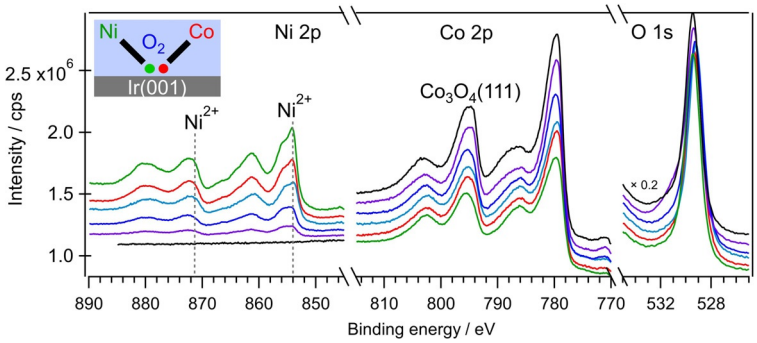

Figure 7. XPS measurements on Co_3O_4(111) (black) and mixed metal-oxide [$Ni_{0.2}Co_{2.8}O_4$ (violet), $Ni_{0.5}Co_{2.5}O_4$ (blue), $Ni_{0.8}Co_{2.2}O_4$ (light blue), $Ni_{1.0}Co_{2.0}O_4$ (red), and $Ni_{1.3}Co_{1.7}O_4$ (green)] thin films generated by simultaneous deposition of Co^0 and Ni^0 in an O_2 atmosphere (see the Experimental Section) on Ir(1 0 0)-(2×1)O. The XP spectra are shown with identical intensity scales, after correction by the sensitivity factors (Ni 2p: 5.4, Co 2p: 4.5, O 1s: 0.63). For better visibility of all spectra, the O 1s peaks were scaled down by a factor of 0.2.

placed by Ni^{2+} and Ni^{3+} cations. Such oxides are known to exist in a spinel structure.[18] The maxima in the Ni 2p range are now located at 854.0 and 871.8 eV (Ni $2p_{3/2}$ and Ni $2p_{1/2}$ peaks, respectively); furthermore, there are pronounced satellite structures at approximately 862 and 879 eV, respectively. In general, in oxides nickel has a preferred oxidation state of +2, as in NiO, but can also adopt states from +1 to +4, for example, in Ni_2O_3, Ni_3O_4, and NiO_2.[46] The Ni 2p peaks and the BEs both of the main peaks and of their satellites look almost identical to those of NiO[47,48] and thus suggest a similar chemical environment of the Ni cations in the mixed oxide film, with Ni in the Ni^{2+} state. A more detailed quantitative analysis of the spectra based on a deconvolution of the different peaks follows below.

Overall, the STM and XPS measurements of the mixed metal-oxide films presented so far revealed 1) the presence of two different phases, with a honeycomb $|\vec{a}| = |\vec{b}| = 0.30 \pm 0.01$ nm and $\alpha = 120 \pm 5°$ surface structure and a commensurate $\begin{bmatrix} 2 & 1 \\ -1 & 1 \end{bmatrix}$ superstructure relative to the honeycomb structure, which are 2) composed of Ni and Co species, and in which 3) Co^{3+} and Co^{2+} cations are increasingly replaced by Ni^{2+} and Ni^{3+} cations with increasing amounts of co-deposited Ni. A possible candidate for these structures could be a nickel-doped cobalt oxide spinel with $Ni_xCo_{3-x}O_4$ stoichiometry.

Comparison of Ni-modified Co_3O_4 thin films

Next, we performed a quantitative analysis of the Ni 2p, Co 2p, and O 1s core-level spectra of an $Ni_{1.0}Co_{2.0}O_4$ mixed metal oxide film (Figure 8c) and pristine Co_3O_4(111) after postdeposition of Ni (0.5 MLE, Figure 8d) by peak deconvolution. In addition, signals of pristine Co_3O_4(111) (Figure 8a) and for metallic Ni and Co (Figure 8b) are shown as well and were evaluated in the same way for comparison. Note that the intensity of all spectra in Figure 8 was adapted to fit into the panels. For the Ni 2p spectra in Figure 8 (first column) we start with the reference spectrum recorded on metallic Ni (Figure 8b), which shows a

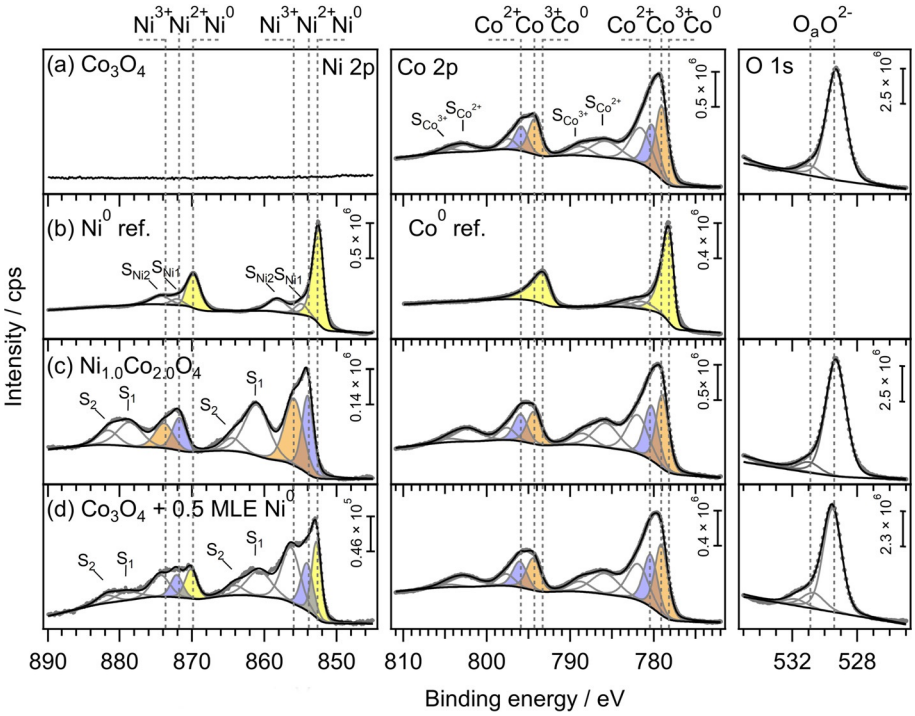

Figure 8. Ni 2p, Co 2p, and O 1s core-level spectra of (a) a Co_3O_4(111) thin film, (b) metallic Ni^0 and Co^0 references, (c) a mixed oxide film, and (d) Co_3O_4(111) after post-deposition of 0.5 MLE of Ni. The intensity of all spectra was adapted to fit into the panels.

© 2020 The Authors. Published by Wiley-VCH Verlag GmbH & Co. KGaA, Weinheim

doublet with peaks at 852.7 and 870.0 eV for the Ni $2p_{3/2}$ and Ni $2p_{1/2}$ states, respectively (see Ref. [45]). In addition, typical satellites are located at 3.7 and 6 eV higher BE (S_{Ni1}, S_{Ni2}) for each peak.[45]

As mentioned above for different $Ni_xCo_{3-x}O_4$ thin films, the Ni 2p spectrum of the $Ni_{1.0}Co_{2.0}O_4$ mixed metal oxide (Figure 8c) looks almost identical to the core-level spectra of NiO (Ni^{2+} state) reported in the literature.[47,48] This typically gives rise to a rather complex line shape, which is often deconvoluted into four peaks[48] for the Ni $2p_{1/2}$ and Ni $2p_{3/2}$ regions, respectively. These include the main peaks (peaks 1) in the Ni $2p_{3/2}$ and Ni $2p_{1/2}$ regions located at 854.0 and 871.7 eV (shaded blue), and broad shoulders at the high-BE side of the main peaks ($\approx +2$ eV, shaded orange, peaks 2) at 855.9 and 873.8 eV. Furthermore, two satellites (peaks 3 and 4, S_1 and S_2) appear at approximately 861 and 863 eV (Ni $2p_{3/2}$) and at 879 and 882 eV (Ni $2p_{1/2}$), respectively (see Ref. [48]). The main peaks appear at a significantly higher BE than the reference peaks of Ni^0 (shaded yellow), and their BEs are in excellent agreement with the expected BEs of Ni^{2+}.[45] This confirms the presence of Ni^{2+} ions in the mixed metal-oxide film, which we expect to be octahedrally coordinated.[47,49] The broad shoulders at the higher-BE side (peaks 2) could originate from overlap of 1) contributions from pyramidally coordinated surface Ni^{2+} cations and nonlocal screening from neighboring oxygen anions (see Refs. [47,49]), or 2) Ni^{3+} states, which are expected at similar BEs of approximately 856 and 874 eV, respectively (see Refs. [46,50]). Finally, 3) also other final-state effects may contribute. Hence, it not possible to unambiguously identify the origin of the broad shoulder at approximately 856 and 874 eV, that is, whether it results from Ni^{2+} or Ni^{3+} cations. Therefore, quantitative evaluation of the ratio between Ni^{2+} and Ni^{3+} ions is hardly possible.

The Ni 2p spectrum of $Co_3O_4+0.5$ MLE Ni (Figure 8d) shows clear maxima at 852.7 and 870.0 eV (shaded yellow), that is, at the same BE as the reference spectrum of metallic Ni (Figure 8b, peaks shaded yellow). Hence, post-deposition of Ni on the $Co_3O_4(111)$ film results in the growth of metallic Ni^0 structures. However, the spectrum also shows additional broad features at the high-BE side of each Ni^0 peak, which are not typical for metallic Ni. The additional features more resemble those of NiO. Apparently, the Ni 2p region contains also contributions from NiO. Oxidic Ni^{2+} species may form, for example, at the interface between $Co_3O_4(111)$ and metallic Ni. We note that the contribution of these additional features in the Ni 2p region decreases with increasing amount of post-deposited Ni^0, owing to damping of these species by increasing amounts of Ni^0, which is clearly visible in the waterfall plot in Figure 5. This supports our assignment that these species are related to ionic Ni species at the interface between the oxide film and the metallic Ni deposit.

The Co 2p core-level spectra of the $Co_3O_4(111)$ film (Figure 8a, second column) are shown for comparison with the Ni-modified oxide films. The signals were fitted with a ratio of 2:1 for the Co^{3+}/Co^{2+} peaks (see also Figure 2 and discussion above). In addition, we show a Co 2p spectrum of metallic Co^0 (Figure 8b, second column), prepared by vapor deposition on Ru(0001) in UHV at RT.[39] This shows a doublet at 778.5 and 793.5 eV (see Refs. [38,39]). Comparison with the other Co 2p spectra in Figure 8 demonstrates that Co^0 states do not contribute to the oxide films presented in this figure.

For the spectrum recorded on the $Ni_{1.0}Co_{2.0}O_4$ mixed oxide thin films, the Co 2p region differs only very little from that of Co_3O_4. The only difference seems to be that the $S_{Co^{2+}}$ satellite is now more prominent compared with $Co_3O_4(111)$. In addition, the pronounced maxima observed for the $Co_3O_4(111)$ film appear a bit smoother. The same is true after post-deposition of metallic Ni on $Co_3O_4(111)$ (Figure 8d). Both changes indicate an increasing amount of Co^{2+} relative to Co^{3+}. Hence, for the peak deconvolution we allowed the relative amount of Co^{3+}/Co^{2+} to change in favor of Co^{2+}, both for the $Ni_{1.0}Co_{2.0}O_4$ mixed oxide films (Figure 8c) and the $Co_3O_4(111)+0.5$ MLE Ni^0 thin film (Figure 8d). Nevertheless, both Co charge states are still present, which clearly speaks against complete transformation of $Co_3O_4(111)$ into a kind of rock salt structure (only Co^{2+}). For the peak deconvolution of the Co 2p spectra, we obtained a good fit for Co^{2+}/Co^{3+} cation ratios of 1:2 in Co_3O_4, and of approximately 1:1.3 in $Ni_{1.0}Co_{2.0}O_4$ and in $Co_3O_4+0.5$ MLE of Ni. For the latter, this indicates that overgrowth with metallic Ni also leads to reactive modification of the Co_3O_4 substrate at the interface. For these fits we adjusted the intensity of the $S_{Co^{2+}}$ satellite such that the intensity ratio of the Co^{2+} main peak to the $S_{Co^{2+}}$ satellite was as in pristine Co_3O_4.

In the O 1s region, the dominant peaks are caused by O^{2-} species at 529.3 eV for all oxide films, except for a low-intensity shoulder at the high-BE side, which we tentatively assign to adsorbed oxygen (O_a, see Figure 2 and related text).

In total, comparison of the Ni 2p, Co 2p, and O 1s core-level spectra of the $Ni_{1.0}Co_{2.0}O_4$ mixed metal-oxide (Figure 8c) and $Co_3O_4+0.5$ MLE Ni thin films (Figure 8d) with those of a pristine $Co_3O_4(111)$ film (Figure 8a) reveals rather similar Co 2p and O 1s spectra for all samples, except for a small decrease of the Co^{2+}/Co^{3+} ratio of 1:2 in Co_3O_4 to approximately 1:1.3 in the Ni-containing surfaces, indicating a relative loss in Co^{3+} species in the latter films and thus a change in the composition of the $Co_3O_4(111)$ substrate near the interface. Clear differences, however, are observed in the Ni 2p signals of the Ni-containing films. They show a complex shape, with Ni^{2+} and Ni^{3+} but no Ni^0 contributions for the $Ni_{1.0}Co_{2.0}O_4$ mixed oxide thin film, whereas after post-deposition of Ni we observe significant amounts of Ni^0. The loss in cationic Co^{3+} charge in these films may be compensated by the presence of ionic Ni species (Ni^{2+}, Ni^{3+}). For the Co_3O_4 films modified with 0.5 MLE Ni, the cationic Ni species are presumably localized at and below the $Co_3O_4|Ni^0$ interface, with a local loss of Co^{3+} in that region.

Electrochemical characterization of Ni-modified Co_3O_4

Before exploring the ORR/OER behavior of the catalyst films we characterized the electrochemical properties in N_2-saturated 0.5 M KOH electrolyte (Figure 9). In the electrochemical measurements we focused on well-defined pure Co_3O_4, Ni-dec-

© 2020 The Authors. Published by Wiley-VCH Verlag GmbH & Co. KGaA, Weinheim

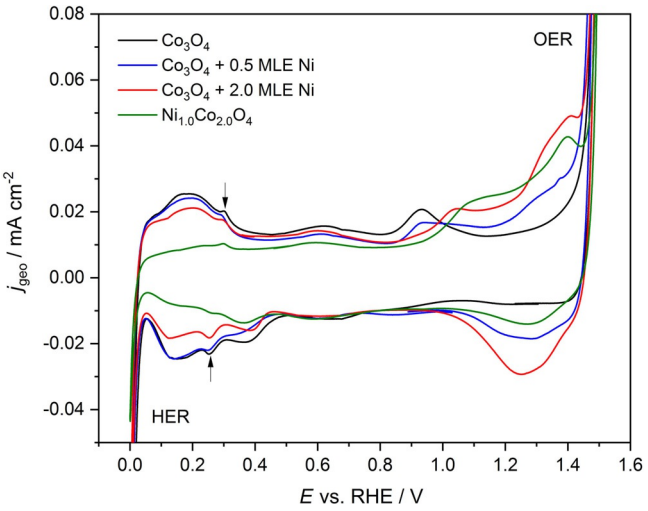

Figure 9. CV of Co_3O_4, Co_3O_4+Ni (0.5 and 2.0 MLE), and of the mixed oxide ($Ni_{1.0}Co_{2.0}O_4$) in N_2-saturated 0.5 M KOH, 10 mV s^{-1}.

orated Co_3O_4 (0.5 and 2.0 MLE of Ni), and $Ni_{1.0}Co_{2.0}O_4$ film electrodes. All electrodes, except the mixed oxide one, show a distinct feature in the potential range of 0.03–0.45 V, which in principle can be related to hydrogen underpotential adsorption/desorption (H_{UPD}), OH^- adsorption/desorption on the surface,[17] and/or oxidation and reduction processes of the surfaces. Because the signals in this region are independent of the presence of metallic Ni at the surface, we attribute them to surface oxidation/reduction and adsorption/desorption processes on the Co_3O_4 film. This assignment is supported by the fact that for the $Ni_{1.0}Co_{2.0}O_4$ mixed oxide these features are absent. From the fact that these signals are observed also on the 2 MLE Ni-covered electrode, albeit with lower current density, we conclude that after cycling this film no longer fully covers the Co_3O_4. At 0.23 V in the cathodic and 0.25 V in the anodic scan, all film electrodes show a small signal, which arises from the H_{UPD} of the underlying Ir(1 0 0) surface (Figure 9, marked by arrows) used as template for oxide film growth in this work (see Figure 1). Hence, from an electrochemical point of view, the Ir(1 0 0) surface is still visible and might influence the ORR/OER measurements (see discussion below). This contribution from the Ir(1 0 0) substrate may arise from small cracks in the oxide films, induced, for example, by the sealing ring in the electrochemical flow cell. Faisal et al. detected facile dissolution of Co (and formation of holes) on Co_3O_4(1 1 1) films in phosphate buffer at pH $\leq$ 8 by scanning flow cell inductively coupled plasma mass spectrometry (SCF-ICP-MS), whereas almost no dissolution occurred at pH values of 10 and 12.[22] Therefore, under the given conditions (KOH, pH 13.7, 0.0–1.5 V_{RHE}) such effects are unlikely, although we cannot exclude them. On decreasing the potential below 0.02 V the current densities increase drastically owing to the formation of H_2 in the HER. Therefore, we chose 0.0 V as the lower potential limit for the CVs.

At higher potentials we found rather constant current densities between 0.45 and 0.8 V for all electrodes, which indicate dominant pseudocapacitive charging of the interface layer (note that pseudocapacitive currents are superimposed on all electrochemical processes). Upon going to higher potentials, the signals differ significantly for the different film electrodes. For the pure and the Ni (0.5 MLE)-covered Co_3O_4 electrode we find a first peak at approximately 0.93 V in the anodic scan, which must be related to the oxidation of Co_3O_4, whereby, for example, Co^{2+} (in Co_3O_4) is oxidized to Co^{3+}, forming CoOOH.[51,52] For the $Ni_{1.0}Co_{2.0}O_4$ mixed oxide film and the Co_3O_4 film electrode covered with larger amounts of Ni (2.0 MLE), this peak is shifted to higher potentials ($\approx$1.0–1.1 V). For the mixed oxide and 2.0 MLE Ni-covered Co_3O_4, this points to a distinct Ni-induced change in the surface (electro)chemistry of the oxide. The oxidation of Co^{3+} to Co^{4+}, which was reported by Song et al. to occur at approximately 1.24–1.54 V,[52] could not be detected on any of these electrodes. Two additional oxidation peaks between 1.0 and 1.1 V and at approximately 1.4 V, which are observed on the Ni-containing electrodes, are most likely owing to Ni-induced oxidation of Co^{2+} to Co^{3+}, which is upshifted compared with pristine Co_3O_4, and to the oxidation of Ni^{2+} to Ni^{3+}, respectively.[52] As expected, the Co_3O_4 surface shows none of these Ni-related signals, and they are least pronounced for Co_3O_4 with 0.5 MLE Ni. We cannot exclude, however, that other reduction/oxidation processes in the mixed Ni–Co oxide might be responsible for the signal between 1.0 and 1.1 V. Finally, in the range of the anodic potential limit, at potentials above 1.4 V, we suggest that the formation of O_2 (OER) results in the steeply increasing currents.

In the cathodic scan the oxidized surfaces are reduced again with a broad signal between 1.4 and 1.0 V. Most prominent is the reduction of the oxidized Ni species (see above), as evident upon comparing the current densities obtained on the Co_3O_4 electrode, which basically only shows pseudocapacitive currents and no reduction currents, with those of the Ni-containing electrodes. Qualitatively, the reduction signal scales with the Ni content in the surface region of the respective electrodes, with the highest current densities for the Ni-covered Co_3O_4 catalyst with 2.0 MLE, lower current densities for that covered with 0.5 MLE Ni, and even lower current densities for the mixed oxide. The lower current densities in this potential region in the cathodic scan compared to the anodic scan obtained for the mixed oxide, even when considering contributions from the OER, furthermore point to severe kinetic limitations in the reduction of the oxidized electrode surface.

In total, upon comparing the results obtained for the structurally and chemically well-defined model electrodes with findings from the 3D materials (Co_3O_4/NiO core–shell nanowire arrays) of Wu et al.[51] and Song et al.,[52] we find rather similar features at higher potentials (>0.8 V) with comparable oxidation and reduction peaks in the materials containing both elements. For Ni-free Co_3O_4, however, we did not observe the formation of CoO_2 at high potentials, as was reported for mesoporous Co_3O_4;[52] that is, structural effects hinder the further oxidation of the structurally compact and well-defined Co_3O_4 films. These films are likely to be roughened on oxidation–reduction cycles, but still much less defective than the mesoporous oxides. The main difference between the mesoporous materials and the structurally well-defined materials investigated

© 2020 The Authors. Published by Wiley-VCH Verlag GmbH & Co. KGaA, Weinheim

here is the absence of any distinct features in the lower-potential region (<0.5 V) for the catalysts. These features, which might be caused by hydrogen and/or hydroxyl adsorption and desorption, seem to be only present on our structured Co_3O_4 surface. This enhanced adsorption/desorption, in comparison to the behavior of the mixed Co–Ni oxides, can strongly influence the ORR and OER processes, which are characterized next.

Figure 10a shows magnified anodic OER scans of the different electrodes, including a scan with a Pt_{poly} reference electrode. Because the OER overlaps with the Ni oxidation reaction, as described above, quantitative determination of the OER onset is not possible. Therefore, we used the potential at 0.1 mA cm^{-2} as a measure of the OER activity of the different electrode materials. By this definition, the Co_3O_4 film covered with 0.5 MLE Ni is most active for the OER (1.46 V at 0.1 mA cm^{-2}). The Ni-free Co_3O_4 film electrode and that covered with 2.0 MLE Ni are rather similar, with slightly higher OER activity (1.47 V at 0.1 mA cm^{-2}), followed finally by the mixed oxide electrode with approximately 1.48 V at 0.1 mA cm^{-2}. All of these oxide film electrodes are, however, considerably more active than the Pt_{poly} reference electrode, by approximately 0.1 V (1.58 V at 0.1 mA cm^{-2}). The OER onset on these film electrodes seems to be significantly lower than those reported for $NiCo_2O_4$ rods over Co_3O_4 nanosheets,[53] Co_3O_4-C on Ni foam,[54] and $NiCo_2O_4$.[18] Note, however, that the current densities in those studies were much larger than those obtained for the film electrodes in our flow-cell setup, which makes a quantitative determination of the potential at 0.1 mA cm^{-2} essentially impossible. Therefore, a quantitative determination of the OER onset values is hardly possible. Considering the different definitions of the onset potential, the discrepancies between the OER onset values are expected to be smaller. However, Zhao et al.[55] presented Co_3O_4/oCNT (oxidized carbon nanotube) catalysts with an OER onset comparable to that of our Co_3O_4 catalyst, when considering the catalyst loading. Sennu et al.[53] showed that the OER onset values of their pure and Ni-modified Co_3O_4 electrodes do not differ significantly. This result is in accordance with literature stating that the ability to surface-oxidize Co_3O_4 is key for the improved OER performance, and not the Ni modification itself.[52]

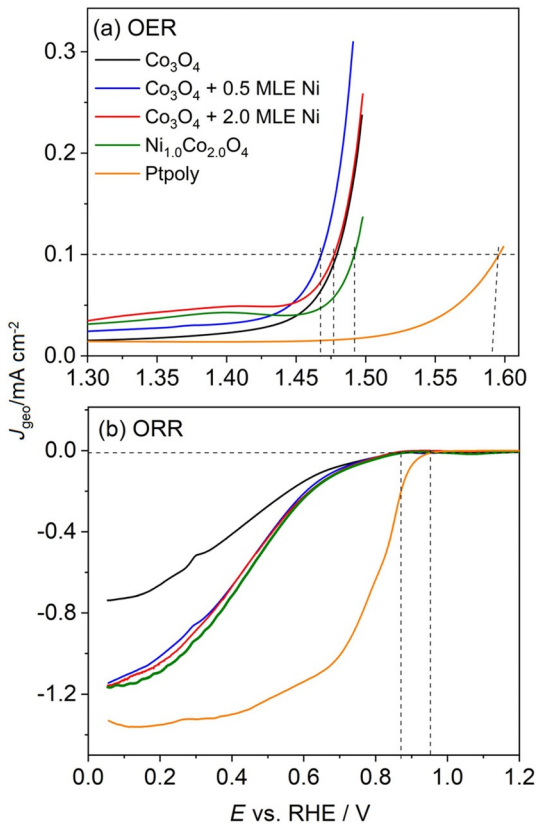

Figure 10. (a) OER and (b) ORR of Co_3O_4, Co_3O_4 + Ni (0.5 and 2.0 MLE), mixed oxide ($Ni_{1.0}Co_{2.0}O_4$), and Pt_{poly} reference in nitrogen-saturated 0.5 M KOH, 10 mV s^{-1}, anodic scan.

Figure 10b summarizes the results of the ORR measurements for the different oxide film electrodes, including the reference Pt_{poly} electrode. Here, we used the potential at 0.01 mA cm^{-2} as measure of the ORR activity of the different electrode materials. The Pt_{poly} electrode has an ORR onset of approximately 0.95 V, in agreement with expectations for a Pt electrode,[56] and reaches a mass-transport-limited current density of approximately −1.4 mA cm^{-2} at approximately 0.4 V, as is known for Pt-based catalysts.[56] The oxide film electrodes in contrast show a slightly higher overpotential, with an onset of the ORR at approximately 0.88 V (potential of 0.01 mA cm^{-2}). Furthermore, different from Pt_{poly}, the oxide electrodes did not reach the diffusion-limited current in the potential range investigated, with the Co_3O_4 electrode showing the lowest current densities at all potentials, while having the same onset as the Ni-modified catalysts. Apparently, the current densities benefit from the Ni doping. This, however, does not seem to go along with a higher electrochemical surface area, as derived from the hydrogen/hydroxyl adsorption/desorption charges in Figure 9, which show similar current densities and thus charges for the pure Co_3O_4 and the Ni-doped film electrodes. Thus, assuming similar maximum coverages of adsorbed species, their surface area should be approximately the same. The current-density differences in the ORR may be explained by the low electronic conductivity of the pure Co_3O_4 film, which is improved by Ni modification, independent of whether this occurs by Ni deposition on top of the Co_3O_4 film or during film growth (mixed oxide).

The slightly higher ORR overpotentials compared with Pt_{poly} are comparable to recent findings for other Co/Ni-oxide-containing electrodes including $NiCo_2O_4$ rods on Co_3O_4 nanosheets,[53] Ni-modified mesoporous Co_3O_4,[52] $NiCo_2O_4$,[18] and $NiCo_2O_4$-based catalysts.[57] This is true also in comparison with exclusively Co-containing oxides such as Co_3O_4 catalyst electrodes,[55] Co_3O_4/oCNT catalysts, and others.[52,58,59] Hence, there is essentially no effect of the Ni modification on the onset of the ORR.[52,55,55–59]

Wang et al.[60] reported Co_3O_4-based electrodes with ORR activity in alkaline electrolyte comparable to that of Pt/C when it was combined with graphene oxide, which also increases the electrical conductivity of the catalyst. Comparable results reported by another group also showed that the ORR activity

© 2020 The Authors. Published by Wiley-VCH Verlag GmbH & Co. KGaA, Weinheim

(onset and currents) of Co_3O_4 nanorods could be improved by addition of conducting materials such as reduced graphene oxide.[61] The influence of adding Ni to Co_3O_4 was also explored by Song et al.[52] in an investigation of Ni-modified mesoporous Co_3O_4, who detected an increase of the current densities in the ORR on addition of Ni, while the ORR onset was maintained. Hence, they concluded that the increased ORR activity is caused by an increase of the surface oxygen defects and surface area, which might also be feasible for our catalysts (see also the above discussion of the OER).

Even though for all Pt-free catalysts the onset of mass-transport limitations is observed in the potential range explored here, the final mass-transport-limited current densities are not reached. This may be owing to conductivity problems or chemical modification of the surface in this potential range. Because the Ni modification does not lead to a shift of the ORR onset and results in similar kinetics, we do not think that the Ni modification plays a major role in the catalytic ORR properties itself, but rather improves the measured rates by increasing the electrical conductivity. This conclusion is in accordance with those in previous reports.[52] Additionally, we detected contributions of the underlying iridium substrate, evidenced by the small peak at approximately 0.3 V, which is similar to that observed in the CVs in N_2-saturated electrolyte. Control experiments performed with pure Ir(1 0 0) showed an ORR onset at approximately 0.67 V (see Figure S1 in the Supporting Information), which is much lower than the onset at 0.88 V obtained for the oxide thin-film electrodes. Thus, we can exclude that the Ir(1 0 0) substrate plays a major role in the measured ORR activity of the oxide films.

Interestingly, the pronounced structural differences between the different Ni-modified electrodes shown above, which resulted in clear differences in the CVs in N_2-purged supporting electrolyte (Figure 9), have little influence on the ORR and OER activity (see Figure 10). Even though the CVs show clear changes in the presence of Ni at potentials higher than 0.7 V, this does not seem to play a major role in the chemistry of the ORR and OER, and it mainly improves the electrical conductivity of the electrodes.

Finally, XP spectra recorded after the electrochemical measurements revealed that all peaks related to the oxide thin-film electrodes are strongly damped. Furthermore, new peaks arise in the O 1s and K 2s region at BEs of 530.8 and 377.9 eV, respectively, which are most likely owing to KOH electrolyte covering the surface (note that the low-intensity peak at ≈532 eV in the O 1s region might be caused by adsorbed water). As an example, we show spectra recorded before and after the electrochemical measurements on a Co_3O_4 film in Figure S2 in the Supporting Information. On the basis of the absence of characteristic changes in the film-related peaks, including their relative intensities, we conclude that the electrochemical measurements did not induce significant changes in the surface composition. Structural changes on an atomic scale cannot be ruled out because it was not possible to gain atomic-scale structural information after the electrochemical measurements from STM imaging owing to the presence of mobile adsorbed species on the surface.

Conclusions

From the preparation of structurally and chemically well-defined pure Co_3O_4, Ni-decorated Co_3O_4, and Ni-doped spinel-type Co_3O_4 films, such as $Ni_{1.0}Co_{2.0}O_4$, their electrochemical characteristics, and their electrocatalytic properties in the oxygen reduction and evolution reactions (ORR/OER), we arrive at the following main results and conclusions:

Co_3O_4(1 1 1) spinel-type thin oxide films prepared by simultaneous dosing of Co^0 and O_2 on Ir(1 0 0) at RT exhibit the expected pure Co^{2+} and Co^{3+} states with a 1:2 ratio in the Co 2p core-level spectra. Scanning tunneling microscopy (STM) revealed extended flat island structures. The atomic-resolution STM images showed a hexagonal unit cell with lattice vectors $|\vec{a}| = |\vec{b}| = 0.57 \pm 0.03$ nm, which enclose an angle of $\alpha = 120 \pm 5^\circ$, in excellent agreement with previous reports.[27]

Exposure of pristine Co_3O_4(1 1 1) to stepwise-increasing amounts of Ni^0 [≈0.2–2 monolayer equivalents (MLE)] leads to a dominant peak in the Ni 2p spectra owing to adsorbed Ni^0. In addition, for the Co_3O_4 films modified with 0.2–0.5 MLE Ni, oxidic Ni^{2+} species may form and are presumably localized at and below the $Co_3O_4|Ni^0$ interface.

Simultaneous deposition of Co^0, Ni^0, and O_2 leads to the formation of mixed metal-oxide thin films. Peak-area analysis of the Ni 2p, Co 2p, and O 1s core-level spectra on deposition of stepwise-increasing amounts of Ni^0 at a constant Co^0 and O_2 flux pointed to a nickel-doped cobalt-oxide spinel with a $Ni_xCo_{3-x}O_4$ stoichiometry, in which Co^{3+} and Co^{2+} cations are increasingly replaced by Ni^{2+} and Ni^{3+} cations with increasing amounts of co-deposited Ni^{3+}, so that the charge balance is maintained and the Co^{3+}/Co^{2+} ratio decreases. The corresponding STM images of the mixed metal-oxide films revealed the presence of two different phases, with a honeycomb $|\vec{a}| = |\vec{b}| = 0.30 \pm 0.01$ nm and $\alpha = 120 \pm 5^\circ$ surface structure and a commensurate $\begin{bmatrix} 2 & 1 \\ -1 & 1 \end{bmatrix}$ superstructure to that phase.

The base cyclic voltammograms of Co_3O_4(1 1 1), Ni-decorated Co_3O_4(1 1 1) (0.5 and 2 MLE), and $Ni_{1.0}Co_{2.0}O_4$ thin films show similarities but also clear differences at potentials higher than 0.7 V.

For Co_3O_4(1 1 1) and Ni-decorated Co_3O_4(1 1 1) (0.5 and 2 MLE), distinct features in the potential range of 0.03–0.45 V are attributed to surface oxidation/reduction and hydrogen/hydroxyl adsorption/desorption processes on the Co_3O_4 film, which are absent for $Ni_{1.0}Co_{2.0}O_4$ thin films.

Furthermore, for the Co_3O_4(1 1 1) and Co_3O_4(1 1 1) + 0.5 MLE Ni^0 thin films, the peak at approximately 0.93 V in the anodic scan must be related to the oxidation of Co_3O_4, whereby, for example, Co^{2+} (in Co_3O_4) is oxidized to Co^{3+}, forming CoOOH, which is absent for the Co_3O_4(1 1 1) + 2 MLE Ni^0 and $Ni_{1.0}Co_{2.0}O_4$ thin films.

For the Ni-decorated (0.5 and 2 MLE) and $Ni_{1.0}Co_{2.0}O_4$ thin films, two additional oxidation peaks between 1.0 and 1.1 V and at approximately 1.4 V are obtained. They are attributed to Ni-induced oxidation of Co^{2+} to Co^{3+}, which is upshifted compared to pristine Co_3O_4, and to the oxidation of Ni^{2+} to Ni^{3+},

© 2020 The Authors. Published by Wiley-VCH Verlag GmbH & Co. KGaA, Weinheim

respectively. In the cathodic scan a prominent reduction peak is present at approximately 1.3 V.

The OER measurements revealed onsets of 1.46 V at 0.1 mA cm^{-2}for the Co_3O_4(111) film covered with 0.5 MLE Ni, 1.47 V at 0.1 mA cm^{-2} for Co_3O_4 and 2.0 MLE Ni-decorated Co_3O_4, and 1.48 V at 0.1 mA cm^{-2} for the $Ni_{1.0}Co_{2.0}O_4$ film mixed oxide electrode. Hence, all of these oxide film electrodes are similarly active and considerably more active than the Pt_{poly} reference electrode.

The ORR measurements for the Co_3O_4(111), Ni-decorated Co_3O_4, and $Ni_{1.0}Co_{2.0}O_4$ oxide thin-film electrodes revealed a common onset at approximately 0.88 V at 0.01 mA cm^{-2}, that is, at higher overpotential than the reference Pt_{poly} electrode ($\approx$0.95 V). Furthermore, the current densities benefit from the Ni doping. Most likely this is related to the rather low electronic conductivity of the pure Co_3O_4 film, which is improved by Ni modification, rather than a higher electrochemically active surface area, as derived from the hydrogen/hydroxyl adsorption/desorption charges. The extent of the Ni modification is independent of whether Ni deposition occurs on top of the Co_3O_4 film or during film growth (mixed oxide).

Overall, the present work clearly illustrates molecular-scale details that can be obtained in such a combined surface science and electrochemical approach, and its potential for improved understanding of the oxygen chemistry taking place at the interface between thin-film oxide (model) electrodes and electrolyte, which is essential for the development of improved future metal–air batteries.

Acknowledgements

This work was supported by the Deutsche Forschungsgemeinschaft (DFG) via project BE 1201/22-1 (Zn-air batteries) and via project ID 422053626 (Cluster of Excellence "Post-Li Storage"), and by the German Federal Ministry of Education and Research in the project LiEcoSafe under contract number 03X4636C. The work contributes to the research performed at CELEST (Center for Electrochemical Energy Storage Ulm-Karlsruhe).

Conflict of interest

The authors declare no conflict of interest.

Keywords: electrochemistry · oxygen evolution reaction · oxygen reduction reaction · surface chemistry · thin films

[1] Y. Li, H. Dai, *Chem. Soc. Rev.* **2014**, *43*, 5257 – 5275.
[2] Y. Li, M. Gong, Y. Liang, J. Feng, J.-E. Kim, H. Wang, G. Hong, B. Zhang, H. Dai, *Nat. Commun.* **2013**, *4*, 1805.
[3] J.-S. Lee, S. Tai Kim, R. Cao, N.-S. Choi, M. Liu, K. T. Lee, J. Cho, *Adv. Energy Mater.* **2011**, *1*, 34 – 50.
[4] P. Gu, M. Zheng, Q. Zhao, X. Xiao, H. Xue, H. Pang, *J. Mater. Chem. A* **2017**, *5*, 7651 – 7666.
[5] P. Pei, K. Wang, Z. Ma, *Appl. Energy* **2014**, *128*, 315 – 324.
[6] P. Tan, B. Chen, H. Xu, H. Zhang, W. Cai, M. Ni, M. Liu, Z. Shao, *Energy Environ. Sci.* **2017**, *10*, 2056 – 2080.
[7] K. Wang, P. Pei, Y. Wang, C. Liao, W. Wang, S. Huang, *Appl. Energy* **2018**, *225*, 848 – 856.
[8] J. Pan, Y. Y. Xu, H. Yang, Z. Dong, H. Liu, B. Y. Xia, *Adv. Sci.* **2018**, *5*, 1700691.
[9] L. Jörissen, *J. Power Sources* **2006**, *155*, 23 – 32.
[10] R. Cao, J.-S. Lee, M. Liu, J. Cho, *Adv. Energy Mater.* **2012**, *2*, 816 – 829.
[11] J.-N. Liu, B.-Q. Li, C.-X. Zhao, J. Yu, Q. Zhang, *ChemSusChem* **2020**, *13*, 1529 – 1536.
[12] I. S. Amiinu, X. Liu, Z. Pu, W. Li, Q. Li, J. Zhang, H. Tang, H. Zhang, S. Mu, *Adv. Funct. Mater.* **2018**, *28*, 1704638.
[13] M. Wang, C. Zhang, T. Meng, Z. Pu, H. Jin, D. He, J. Zhang, S. Mu, *J. Power Sources* **2019**, *413*, 367 – 375.
[14] D. Chen, J. Zhu, X. Mu, R. Cheng, W. Li, S. Liu, Z. Pu, C. Lin, S. Mu, *Appl. Catal. B* **2020**, *268*, 118729.
[15] S. Dresp, P. Strasser, *ChemCatChem* **2018**, *10*, 4162 – 4171.
[16] C. Goswami, K. K. Hazarika, P. Bharali, *Mater. Sci. Energy Technol.* **2018**, *1*, 117 – 128.
[17] A. Singhal, A. Bisht, S. Irusta, *J. Electroanal. Chem.* **2018**, *823*, 482 – 491.
[18] M. Prabu, K. Ketpang, S. Shanmugam, *Nanoscale* **2014**, *6*, 3173 – 3181.
[19] J. Schnaidt, S. Beckord, A. K. Engstfeld, J. Klein, S. Brimaud, R. J. Behm, *Phys. Chem. Chem. Phys.* **2017**, *19*, 4166 – 4178.
[20] M. Müllner, M. Riva, F. Kraushofer, M. Schmid, G. S. Parkinson, S. F. L. Mertens, U. Diebold, *J. Phys. Chem. C* **2019**, *123*, 8304 – 8311.
[21] J. Fester, A. Makoveev, D. Grumelli, R. Gutzler, Z. Sun, J. Rodríguez-Fernández, K. Kern, J. V. Lauritsen, *Angew. Chem. Int. Ed.* **2018**, *57*, 11893 – 11897; *Angew. Chem.* **2018**, *130*, 12069 – 12073.
[22] F. Faisal, M. Bertram, C. Stumm, S. Cherevko, S. Geiger, O. Kasian, Y. Lykhach, O. Lytken, K. J. J. Mayrhofer, O. Brummel, J. Libuda, *J. Phys. Chem. C* **2018**, *122*, 7236 – 7248.
[23] Y. Liang, Y. Li, H. Wang, J. Zhou, J. Wang, T. Regier, H. Dai, *Nat. Mater.* **2011**, *10*, 780 – 786.
[24] F. Cheng, J. Shen, B. Peng, Y. Pan, Z. Tao, J. Chen, *Nat. Chem.* **2011**, *3*, 79.
[25] B. Iandolo, A. Hellman, *Angew. Chem. Int. Ed.* **2014**, *53*, 13404 – 13408; *Angew. Chem.* **2014**, *126*, 13622 – 13626.
[26] K. Biedermann, M. Gubo, L. Hammer, K. Heinz, *J. Phys. Condens. Matter* **2009**, *21*, 185003.
[27] W. Meyer, K. Biedermann, M. Gubo, L. Hammer, K. Heinz, *J. Phys. Condens. Matter* **2008**, *20*, 265011.
[28] M. Schwarz, C. Hohner, S. Mohr, J. Libuda, *J. Phys. Chem. C* **2017**, *121*, 28317 – 28327.
[29] K. Anic, A. V. Bukhtiyarov, H. Li, C. Rameshan, G. Rupprechter, *J. Phys. Chem. C* **2016**, *120*, 10838 – 10848.
[30] F. Martin, J. Pacaud, G. Abadias, C. Jaouen, P. Guérin, *Appl. Surf. Sci.* **2002**, *188*, 90 – 96.
[31] C. J. Powell, A. Jablonski, *NIST Electron Inelastic-Mean-Free-Path Database*, 1.1 ed., National Institute of Standards and Technology, Gaithersburg, **2000**.
[32] Z. Jusys, H. Massong, H. Baltruschat, *J. Electrochem. Soc.* **1999**, *146*, 1093 – 1098.
[33] Z. Jusys, R. J. Behm, *J. Phys. Chem. B* **2001**, *105*, 10874 – 10883.
[34] P. Ferstl, T. Schmitt, M. A. Schneider, L. Hammer, A. Michl, S. Müller, *Phys. Rev. B* **2016**, *93*, 235406.
[35] T. Pajkossy, L. A. Kibler, D. M. Kolb, *J. Electroanal. Chem.* **2007**, *600*, 113 – 118.
[36] D. S. Hall, C. Bock, B. R. MacDougall, *J. Electrochem. Soc.* **2014**, *161*, H787 – H795.
[37] I. Bakos, A. Paszternák, D. Zitoun, *Electrochim. Acta* **2015**, *176*, 1074 – 1082.
[38] M. C. Biesinger, B. P. Payne, A. P. Grosvenor, L. W. M. Lau, A. R. Gerson, R. S. C. Smart, *Appl. Surf. Sci.* **2011**, *257*, 2717 – 2730.
[39] F. Buchner, K. Forster-Tonigold, J. Kim, J. Bansmann, A. Groß, R. J. Behm, *Chem. Mater.* **2019**, *31*, 5537 – 5549.
[40] S. C. Petitto, M. A. Langell, *J. Vac. Sci. Technol. A* **2004**, *22*, 1690 – 1696.
[41] T. J. Chuang, C. R. Brundle, D. W. Rice, *Surf. Sci.* **1976**, *59*, 413 – 429.
[42] M. A. Langell, M. D. Anderson, G. A. Carson, L. Peng, S. Smith, *Phys. Rev. B* **1999**, *59*, 4791 – 4798.
[43] J. Fester, M. García-Melchor, A. S. Walton, M. Bajdich, Z. Li, L. Lammich, A. Vojvodic, J. V. Lauritsen, *Nat. Commun.* **2017**, *8*, 14169.
[44] P. Ferstl, S. Mehl, M. A. Arman, M. Schuler, A. Toghan, B. Laszlo, Y. Lykhach, O. Brummel, E. Lundgren, J. Knudsen, L. Hammer, M. A. Schneider, J. Libuda, *J. Phys. Chem. C* **2015**, *119*, 16688 – 16699.

 © 2020 The Authors. Published by Wiley-VCH Verlag GmbH & Co. KGaA, Weinheim

[45] A. P. Grosvenor, M. C. Biesinger, R. S. Smart, N. S. Mcintyre, *Surf. Sci.* **2006**, *600*, 1771 – 1779.
[46] E. L. Ratcliff, J. Meyer, K. X. Steirer, A. Garcia, J. J. Berry, D. S. Ginley, D. C. Olson, A. Kahn, N. R. Armstrong, *Chem. Mater.* **2011**, *23*, 4988 – 5000.
[47] I. Preda, A. Gutiérrez, M. Abbate, F. Yubero, J. Méndez, L. Alvarez, L. Soriano, *Phys. Rev. B* **2008**, *77*, 075411.
[48] M. A. Peck, M. A. Langell, *Chem. Mater.* **2012**, *24*, 4483 – 4490.
[49] L. Soriano, I. Preda, A. Gutiérrez, S. Palacín, M. Abbate, A. Vollmer, *Phys. Rev. B* **2007**, *75*, 233417.
[50] S. Oswald, W. Brückner, *Surf. Interface Anal.* **2004**, *36*, 17 – 22.
[51] J. B. Wu, Z. G. Li, X. H. Huang, Y. Lin, *J. Power Sources* **2013**, *224*, 1 – 5.
[52] W. Song, Z. Ren, S.-Y. Chen, Y. Meng, S. Biswas, P. Nandi, H. A. Elsen, P.-X. Gao, S. L. Suib, *ACS Appl. Mater. Interfaces* **2016**, *8*, 20802 – 20813.
[53] P. Sennu, H. S. Park, K. U. Park, V. Aravindan, K. S. Nahm, Y.-S. Lee, *J. Catal.* **2017**, *349*, 175 – 182.
[54] J.-T. Ren, G.-G. Yuan, C.-C. Weng, Z.-Y. Yuan, *ACS Sustainable Chem. Eng.* **2018**, *6*, 707 – 718.
[55] S. Zhao, B. Rasimick, W. Mustain, H. Xu, *Appl. Catal. B* **2017**, *203*, 138 – 145.
[56] N. Markovic, H. A. Gasteiger, P. N. Ross, *J. Electrochem. Soc.* **1997**, *144*, 1591 – 1598.
[57] D. U. Lee, B. J. Kim, Z. Chen, *J. Mater. Chem. A* **2013**, *1*, 4754 – 4762.
[58] K. Kumar, C. Canaff, J. Rousseau, S. Arrii-Clacens, T. W. Napporn, A. Habrioux, K. B. Kokoh, *J. Phys. Chem. C* **2016**, *120*, 7949 – 7958.
[59] Z. Song, X. Han, Y. Deng, N. Zhao, W. Hu, C. Zhong, *ACS Appl. Mater. Interfaces* **2017**, *9*, 22694 – 22703.
[60] D.-C. Wang, N.-B. Huang, Y. Sun, S. Zhan, J.-J. Zhang, *Int. J. Hydrogen Energy* **2017**, *42*, 20216 – 20223.
[61] M. Wang, J. Huang, M. Wang, D. Zhang, W. Zhang, W. Li, J. Chen, *Electrochem. Commun.* **2013**, *34*, 299 – 303.

Manuscript received: February 25, 2020
Revised manuscript received: March 25, 2020
Accepted manuscript online: March 26, 2020
Version of record online: May 11, 2020

 © 2020 The Authors. Published by Wiley-VCH Verlag GmbH & Co. KGaA, Weinheim